Physics of Fluids

RESEARCH ARTICLE | OCTOBER 25 2022

# Sensitivity analysis on supersonic-boundary-layer stability: Parametric influence, optimization, and inverse design

Peixu Guo (郭培旭) ; Fangcheng Shi (施方成) ; Zhenxun Gao (高振勋) ; Chongwen Jiang (蒋崇文); Chun-Hian Lee (李椿萱) ; Chihyung Wen (温志湧)



*Physics of Fluids* 34, 104113 (2022)
https://doi.org/10.1063/5.0110560

Physics of Fluids ARTICLE scitation.org/journal/phf

# Sensitivity analysis on supersonic-boundary-layer stability: Parametric influence, optimization, and inverse design

Cite as: Phys. Fluids **34**, 104113 (2022); doi: 10.1063/5.0110560
Submitted: 16 July 2022 · Accepted: 21 September 2022 ·
Published Online: 25 October 2022



Peixu Guo (郭培旭),[1,2,a)] Fangcheng Shi (施方成),[1,3] Zhenxun Gao (高振勋),[1,b)] Chongwen Jiang (蒋崇文),[1] Chun-Hian Lee (李椿萱),[1] and Chihyung Wen (温志湧)[2]

## AFFILIATIONS

[1]National Laboratory for Computational Fluid Dynamics, School of Aeronautic Science and Engineering, Beihang University, Beijing 100191, China
[2]Department of Aeronautical and Aviation Engineering, The Hong Kong Polytechnic University, Kowloon, Hong Kong, China
[3]College of Mechanical and Vehicle Engineering, Hunan University, Changsha 410082, China

[a)]Email address: buaaguopeixu@buaa.edu.cn
[b)]Author to whom correspondence should be addressed: gaozhenxun@buaa.edu.cn

## ABSTRACT

Perturbations of flow control parameters may yield a significant alteration in the boundary layer stability. Based on the previously established parameter-associated sensitivity, the present work derives the optimal minor parameter perturbation analytically under the constraint of base flow energy variation. Specifically, the steady blowing-suction factor and the generalized Hartree parameter are examined at Mach number 4.5 to stabilize the mode S. Good agreement between the linear stability theory calculation, sensitivity theory, and Lagrangian approach is achieved for the optimal parametric state. The optimal state occurs if the contribution of the base velocity distortion has the greatest advantage over the temperature counterpart. Contributions of various physical sources to the growth rate behave similarly and collapse onto one correlation if normalized by the maximum, particularly for the major four: advection, mean shear, base temperature gradient, and pressure gradient. When the parameter perturbation further becomes finite, the optimal state is found on the constraint border of control parameters. Although the favorable pressure gradient and wall suction stabilize the broadband mode S, an unusual opposite tendency may occur for a single-frequency disturbance. In this unusual parametric range, positive contributions of both the major and minor physical sources to the growth rate are promoted. The contributive increase in major and minor sources are attributed to the enhancement of mean shear and viscous effect, respectively. Whether the parametric influence is stabilization or destabilization is intrinsically determined by the sensitivities, and the intermediate process is analyzed. Finally, given the modification to the critical Reynolds number, the input control parameter perturbation is inversely obtained and verified.





## I. INTRODUCTION

Boundary layer transition in high-speed flows can appreciably affect the aircraft design of the aerodynamic shape and thermal protection system. To accurately predict or control transitional flows is substantially challenging due not only to the fact that the flow mechanism is far from being fully understood, but also that the transition location is highly sensitive to potential external perturbations. Recently, sensitivity analyses based on the adjoint equations have thrown new light on the methodology for parametric studies or optimal control on the boundary layer stability. In a concerned dynamic system, sensitivity analytically presents the response of an objective function with respect to perturbations of variables or parameters. By utilizing the adjoint method, the sensitivity of the objective, say the growth rate of boundary layer disturbances, to a series of input variables is obtained immediately and simultaneously. Thus, the adjoint-based sensitivity analysis would largely save the computational cost of parametric investigations.

In the past three decades, adjoint-based sensitivity analysis has been mostly applied in obtaining the optimal input field variables and revealing the dominant physical effect. Within the scope of the flow stability, the specialized issues are broadly distributed from the natural receptivity of Tollmien–Schlichting (T–S) waves,[1] the localized

receptivity[2,3] of T–S waves, the receptivities of Mack second mode,[4] Görtler instability[5] and attachment line instability,[6] the global primary and secondary instability sources of wake flows[7,8] together with the feedback control[9] and the optimal disturbance in the transient growth.[10,11] Early important knowledge is that the receptivity coefficient (complex output) equals the adjoint variables or their integral for concentrated or distributed sources, respectively.[2,3] Meanwhile, forcing in the vicinity of the critical layer generates the most pronounced response of disturbances in the boundary layer. For instabilities initiating from the leading edge, global stability and sensitivity analyses of the swept wing[6] and the swept blunt body[12] in the compressible flow demonstrated that the global eigenfunction is the most sensitive to the forcing near the attachment line. In terms of the global instability occurring in the wake past a circular cylinder, the perturbation in the identified spatial region called "wave maker" affects the response frequency mostly, while the remaining domain serves as an amplitude amplifier.[7] Contributions are also seen in the optimal disturbance in the temporally transient growth[13,14] or in the spatial algebraic and exponential growths.[10,15,16] Recently, the nonlinear input–output analysis has been used to obtain the disturbance that maximizes the drag and triggers the breakdown.[17] These studies have shed new insight into the optimal variables including the forcing or the self-sustained disturbance.

Another origin of the stability alteration is the base flow distortion (BFD). The BFD can result in the uncertainty of the transition location and participate in nonlinear wave interactions effectively. Sensitivity analyses demonstrated that the BFD significantly affects the convective instability[18,19] and absolute instability,[20] and the optimal BFD can be given within the neighborhood. Here, a flow is absolutely unstable if its response to perturbations becomes unbounded for large time in the entire domain, e.g., the self-sustained unstable wake flow. By contrast, a flow is convectively unstable if the disturbance is convected away and the response decays to zero for large time, e.g., the unstable boundary layer initiated by the T–S wave. Brandt *et al.*[21] found that the BFD has a rare impact on the transient growth compared to the modal T–S wave instability. With respect to the high-speed flows, Park and Zaki[19] showed that mode S at Mach number 4.5 is more responsive to the base velocity distortion than the temperature counterpart, and the contributions to the growth rate can be decomposed into various physical mechanisms. Here, mode S and mode F, also known as the slow mode and fast mode, were introduced in detail in the terminological framework of Fedorov and Tumin.[22] The phase-speed synchronization between modes S and F is found to be responsible for the presence of Mack second mode instability, which is significant in the boundary layer with Mach number exceeding around 4. In most common cases, the low- and high-frequency maximum growth rates of mode S correspond to the traditional first mode and Mack second mode, respectively. In terms of the engineering background, the sensitivity as well as the control strategy[23,24] of the boundary layer stability of a high-speed cruise vehicle is of widespread interest. However, less attention has been paid to obtaining the optimal factors which are compactly represented by dominant flow parameters in the overall design of vehicles, such as the Mach number and wall blowing-suction factor. These dimensionless parameters, rather than field variables that were previously concentrated on, have merits in characterizing the flow condition and the ability to be applied in iterative engineering designs straightforwardly and efficiently. Guo *et al.*[25] established the analytical relationship between the input parameter perturbations and the output growth rate variation using the homotopy analysis for the base flow solution and the direct-adjoint analysis by Park and Zaki.[19] The parameter perturbation can give rise to the change in the linear stability theory (LST) eigenvalue via either the BFD or the linear operator distortion.

The present study is inspired by our previously established formula of sensitivity,[25] which describes the response of the boundary layer stability to perturbations of dimensionless flow parameters. Proceeding from this formula, the optimal dimensionless parameters under certain energy constraint are analytically derived in the present paper. In addition to giving the optimal parameters, the present work reveals the underlying mechanism on why the presented parameter perturbations induce the largest response of the LST eigenvalue. Another current state is that adjoint-based forward design shows how the output growth rate changes with the input parameter perturbation. However, the inverse design problem related to the high-speed flow stability receives much less attention. The established inverse design procedure can figure out the input parameter perturbations given the modification to the critical Reynolds number.

Active flow control for the boundary layer stability can be achieved by the introduction of the wall blowing or suction[26–28] or pressure gradient alteration by the continuous shape adjustment.[29] The steady blowing-suction factor $V_w$ and the pressure gradient factor $\beta_H$ are considered as the input control parameters in the present paper. In Sec. II, the physical and mathematical background and brief review of the parameter-associated sensitivity theory are presented. In Sec. III, the analytical approaches of the parametric optimization and inverse design are introduced. In Sec. IV, the results and discussions are provided. Finally, the concluding remarks are given.

## II. BACKGROUND AND REVIEW OF THE PARAMETER-ASSOCIATED SENSITIVITY THEORY

This section provides an overview of the physical and mathematical background and the sensitivity theory in the part I work.[25] This will serve as a foundation of the theoretical derivation for both optimization and inverse design. Basically, the terminology "sensitivity" describes the modification to the system state as a response to variations of parameters or field variables. With the explicit expressions of the sensitivity, the systemic responses to the considered parameter perturbations can be immediately obtained without repeated calculations.

In the convective instability problem, we perform a locally parallel-flow analysis, where the base state possesses the form as

$$U = U(y), \quad V = 0, \quad W = W(y), \quad T = T(y), \quad \rho = \rho(y). \tag{1}$$

Here, $U$, $V$, and $W$ are the base velocity components in the Cartesian coordinate system, $T$ and $\rho$ are temperature and density, respectively, and $y$ denotes the wall-normal coordinate. Meanwhile, consider the boundary layer disturbance with the normal mode assumption,

$$\phi(x, y, z, t) = \boldsymbol{\varphi}(y) e^{\mathrm{i}(\alpha x + \beta z - \omega t)} + \text{c.c.}, \tag{2}$$

where $\boldsymbol{\varphi}$ denotes the eigenfunction of the LST eigenvalue problem, and the symbols $\alpha$, $\beta$, and $\omega$ denote the streamwise wavenumber, spanwise wavenumber, and angular frequency, respectively, while c.c. refers to the complex conjugate. With respect to the spatially propagating instability wave, the minus imaginary part $-\alpha_i$ is the spatial growth rate of the eigenmode. For convenience, we define $\sigma = \mathrm{i}\alpha$ so that the growth rate $\sigma_r > 0$ refers to the unstable mode. If the output

$\delta\sigma_r < 0$ in response to the input parameter perturbations, the flow tends to be locally more stable. Usually in the aerodynamic design of hypersonic vehicles, the desired flow state is to ensure the stabilization of Mack modes as far as possible. Hereupon, the active flow control strategies are popular solutions to be introduced in order to delay the amplification of dominant modes.

Mathematically, for convenience of description, the symbols $\boldsymbol{\mathcal{M}}$ and $\boldsymbol{\mathcal{Q}}$ are referred to as vectors of dimensionless flow control parameters and base-flow quantities, respectively. As a representative example, the considered flow control parameters are specified in this paper as $\boldsymbol{\mathcal{M}} = (V_w, \beta_H)^{\mathrm{T}}$. Here, the superscript "T" denotes the transpose. The symbols $V_w$ and $\beta_H$ denote the steady blowing-suction parameter and the generalized Hartree parameter that characterizes the streamwise pressure gradient, respectively. The detailed expressions of $V_w$ and $\beta_H$ will be introduced thereinafter. In the theoretical calculation of this paper, the Mach number is held fixed on the boundary layer edge, while the flow control parameters are adjustable. As for the base flow, the compressible flow can be characterized by the velocity and temperature profiles. Thus, the base flow is given by the dimensionless profiles $\boldsymbol{\mathcal{Q}} = (U, T)^{\mathrm{T}}$ that are nondimensionalized by the corresponding boundary-layer-edge quantities. Other base-flow quantities, e.g., base density $\rho$ and thermodynamic quantities like the dynamic viscosity $\mu$ and thermal conductivity $\kappa$, are accordingly solvable from boundary layer equations and corresponding thermodynamic correlations.

Before deriving the sensitivity expression, the definition of the parameter-associated sensitivity is given first. Let $(\boldsymbol{a}, \boldsymbol{b})$ represent the inner product defined as $\int_0^\infty \boldsymbol{a}^{\mathrm{H}} \cdot \boldsymbol{b} dy$ for the vectors $\boldsymbol{a}$ and $\boldsymbol{b}$, where the superscript "H" represents the conjugate transpose. The parameter-associated sensitivity of the eigenvalue to the perturbation $\delta\boldsymbol{\mathcal{M}}$ is then defined as $\nabla^{\mathrm{e}}_{\boldsymbol{\mathcal{M}}}\sigma$, which satisfies

$$\delta\sigma = (\nabla^{\mathrm{e}}_{\boldsymbol{\mathcal{M}}}\sigma, \delta\boldsymbol{\mathcal{M}}). \tag{3}$$

The above equation establishes the linear relationship between the input $\delta\boldsymbol{\mathcal{M}}$ and output $\delta\sigma$. The $y$-directional integral of the sensitivity $\nabla^{\mathrm{e}}_{\boldsymbol{\mathcal{M}}}\sigma$ can be regarded as the eigenvalue variation response under per unit input perturbation of the parameter $\delta\boldsymbol{\mathcal{M}}$.

To derive the expression of $\nabla^{\mathrm{e}}_{\boldsymbol{\mathcal{M}}}\sigma$, consider the perturbation of the linear stability equation arising from the parameter perturbation $\delta\boldsymbol{\mathcal{M}}$ as well as the resulting base flow distortion $\delta\boldsymbol{\mathcal{Q}}$ and eigenfunction distortion $\delta\boldsymbol{\varphi}$. The linear stability equation can be expressed in the operator form as

$$\boldsymbol{\mathcal{L}}(\sigma, \boldsymbol{\mathcal{Q}}, \boldsymbol{\mathcal{M}})\varphi = 0, \tag{4}$$

where $\boldsymbol{\mathcal{L}}$ is the linear operator. For the commonly concerned most unstable second mode that is two-dimensional (2D) ($\beta = 0$), we specify the eigenvector form as $\boldsymbol{\varphi} = (\hat{u}, \hat{v}, \hat{p}, \hat{T})$. The complete form of the linear stability equation for the 2D Mack mode is provided in the Appendix. Performing a first-order Taylor expansion and approximation and subtracting the original equation (4) from the perturbed state yield

$$\boldsymbol{\mathcal{L}}\delta\varphi + \left(\frac{\partial\boldsymbol{\mathcal{L}}}{\partial\sigma}\delta\sigma + \frac{\partial\boldsymbol{\mathcal{L}}}{\partial\boldsymbol{\mathcal{Q}}}\delta\boldsymbol{\mathcal{Q}} + \frac{\partial\boldsymbol{\mathcal{L}}}{\partial\boldsymbol{\mathcal{M}}}\delta\boldsymbol{\mathcal{M}}\right)\varphi = 0. \tag{5}$$

Thanks to the previously presented homotopy analysis,[25,30] the variations in the flow parameter and the base flow can be linearly correlated. Specifically, with introduction of an embedding parameter $q$, a series solution $\boldsymbol{\mathcal{Q}} = \boldsymbol{\mathcal{Q}}(q, \eta, \boldsymbol{\mathcal{M}})$ can be attained by an expansion of the nonlinear base flow equation with respect to $q$. Then, by setting $q = 1$, the constructed equation reduces to the original one, and thus the series solution gives an explicit approximation to the accurate one. Through the partial derivative operation, the linear correlation is expressed as $\delta\boldsymbol{\mathcal{Q}} = (\nabla_{\boldsymbol{\mathcal{M}}}\boldsymbol{\mathcal{Q}}, \delta\boldsymbol{\mathcal{M}})$. Thus, the intermediate variable $\delta\boldsymbol{\mathcal{Q}}$ in Eq. (5) can be replaced by the input parameter perturbation. Additionally, to eliminate the unknown first left-hand-side (l.h.s.) term of Eq. (5), we perform the inner product of the adjoint variable $\varphi^\dagger$ with Eq. (5). Here, the adjoint variable with the superscript "†" is defined by $(\boldsymbol{a}^\dagger, \boldsymbol{\mathcal{L}}\boldsymbol{b}) = (\boldsymbol{\mathcal{L}}^\dagger\boldsymbol{a}^\dagger, \boldsymbol{b})$ for smooth vectors $\boldsymbol{a}$ and $\boldsymbol{b}$. Accordingly, the first l.h.s. term of Eq. (5) is dropped out based on the adjoint LST equation $\boldsymbol{\mathcal{L}}^\dagger\boldsymbol{\varphi}^\dagger = 0$ that leads to $(\boldsymbol{\varphi}^\dagger, \boldsymbol{\mathcal{L}}\delta\boldsymbol{\varphi}) = (\boldsymbol{\mathcal{L}}^\dagger\boldsymbol{\varphi}^\dagger, \delta\boldsymbol{\varphi}) = 0$. The above manipulation finally yields the $\delta\sigma \sim \delta\boldsymbol{\mathcal{M}}$ relationship for Eq. (4), which is given by

$$\underbrace{\left(\varphi^\dagger, \frac{\partial\boldsymbol{\mathcal{L}}}{\partial\sigma}\varphi\right)}_{\hat{R}}\delta\sigma = \left(\underbrace{-\varphi^\dagger\left(\frac{\partial\boldsymbol{\mathcal{L}}}{\partial\boldsymbol{\mathcal{Q}}}\varphi\right)^\dagger}_{\nabla_{\boldsymbol{\mathcal{Q}}\sigma}}\nabla_{\boldsymbol{\mathcal{M}}}\boldsymbol{\mathcal{Q}}, \delta\boldsymbol{\mathcal{M}}\right) + \left(-\varphi^\dagger\left(\frac{\partial\boldsymbol{\mathcal{L}}}{\partial\boldsymbol{\mathcal{M}}}\varphi\right)^\dagger, \delta\boldsymbol{\mathcal{M}}\right). \tag{6}$$

Since both sides of Eq. (6) are in the form of the dot product of direct and adjoint eigenvectors, proper normalization of eigenvectors allows that $\hat{R} = 1$. Subsequently, the first and second right-hand-side (r.h.s.) terms represent the eigenvalue variation responses due to the BFD and the stability operator distortion because of the parameter perturbation, respectively. The part I work of the authors[25] showed that the contribution of the operator distortion can be significant. However, the discussed parameters $V_w$ and $\beta_H$ in this paper only appear in the base flow equation explicitly instead of the stability operator. In other words, the second r.h.s. term of Eq. (6) vanishes in the considered scenario. Consequently, the only mechanism of the eigenvalue variation should be that the parameter perturbations of $V_w$ and $\beta_H$ serve as the base flow modifier, and thus, the linear stability operator and further the eigenvalues are altered.

The remaining first r.h.s. stability-associated sensitivity in Eq. (6) can be generally divided into the contributions of the base-velocity distortion $\delta U$ and base-temperature distortion $\delta T$, which further consists of different terms in terms of the physical origins from the distorted stability equation. Through the decomposition into various physical mechanisms, the explicit analytical expression of $\nabla_{\boldsymbol{\mathcal{Q}}}\sigma$ is shown in the Appendix, while $\nabla_{\boldsymbol{\mathcal{M}}}\boldsymbol{\mathcal{Q}}$ is given by the homotopy analysis. The formulation and the Mathematica code for homotopy analysis on the self-similar base flow have been completely provided in the Supplementary Material of the part I work,[25] which enables the reproduction of the present results. When the type of the base flow is extended to other self-similar or non-similar ones, homotopy analysis of the base flow can be conducted in a similar manner.

The considered base flow equation and flow parameters are described below. By means of the Levy–Lees transformation,

$$\begin{cases} \xi^* = \int_0^{x^*} \rho_e^*\mu_e^*U_e^* d\tilde{x}^*, \\ \eta = \dfrac{U_e^*}{\sqrt{2\xi^*}}\int_0^{y^*} \bar{\rho}^* d\tilde{y}^*, \end{cases} \tag{7}$$

where the asterisk and the subscript "$e$" denote the dimensional variable and the boundary layer edge quantity, respectively, the two-dimensional steady compressible boundary layer equations can be transformed into the following self-similar form:[25,31]

$$\begin{cases} f''' + ff'' + \beta_H(S - f'^2) = 0, \\ S'' + fS' = 0, \end{cases} \tag{8}$$

where $f$ satisfies $f'(\eta) = U$, $S$ represents the dimensionless total enthalpy and $\beta_H = (2\xi^*/Ma_e)dMa_e/d\xi^*$ is the generalized Hartree parameter associated with the pressure gradient, and $Ma$ is the Mach number. One of the boundary conditions at wall yields the blowing-suction factor, which is expressed by $f_w = V_w = -\int_0^{x^*} \rho_w^* V_w^* d\tilde{x}^* / \sqrt{2\int_0^{x^*} \rho_e^* \mu_e^* U_e^* d\tilde{x}^*}$. Assume that the steady blowing-suction factor $V_w$ is constant downstream of a certain $x_0^*$, which ensures the existence of self-similarity in the concerned region $x^* > x_0^*$. This assumption indicates that wall blowing-suction occurs only in the region $x^* \le x_0^*$. Physically, $V_w > 0$ and $\beta_H > 0$ suggest the presence of the steady wall suction and favorable pressure gradient, respectively. Details including other boundary conditions are accessible in the part I work.[25] The reference length scale for nondimensionalization is $l^* = \sqrt{\xi^*/\rho_e^* u_e^*}$, which reduces to the Blasius scale $\sqrt{\mu_e^* x^*/\rho_e^* u_e^*}$ commonly used in LST analyses in zero-pressure-gradient boundary layers.

The direct-adjoint LST eigenvalue problem is solved by the Chebyshev pseudo-spectrum method to obtain the global eigenvalue spectrum and an iterative compact fourth-order difference scheme to improve the accuracy of the eigenvalue and eigenfunction. The original numerical methods are established by Malik,[32] and the reliability of our LST solver as well as the sensitivity theory is confirmed by calculating a series of benchmark cases.[25,33]

## III. FORMULATION OF THE OPTIMIZATION AND INVERSE DESIGN APPROACHES

### A. Optimization approach

Indicated by the definition of sensitivity Eq. (3), the integral of each sensitivity $\int_0^\infty \nabla^{\mathrm{e}}_{\boldsymbol{\mathcal{M}}_i} \sigma_r dy$ actually constitutes the gradient of the growth rate $\sigma_r$ with respect to parameters written as $(\partial\sigma_r/\partial\boldsymbol{\mathcal{M}}_1, \partial\sigma_r/\partial\boldsymbol{\mathcal{M}}_2, \dots)$. The gradient represents the optimal direction of the parametric design in which the growth rate varies the fastest in an infinitesimal neighborhood of the initial state. Previous studies[18,19] have given the optimal distortion of local base-flow profiles. However, the analytical optimal base-flow profile does not satisfy the boundary layer equation.[19] This point can be overcome if the optimization procedure is performed with respect to the dimensionless parameter, which is simply because the optimal increment is indirectly calculated for the parameter rather than the base-flow profile. Immediately after the optimal parameter is obtained, the updated base flow is solved from the boundary layer equation. Therefore, the optimal $U$ and $T$ are naturally in accordance with the boundary layer condition. When the required optimal parameter $\widetilde{\boldsymbol{\mathcal{M}}}$ is potentially away from the initial state $\boldsymbol{\mathcal{M}}$, the optimization procedure should be repeated iteratively till the optimization objective is fulfilled. The optimization objective is, for instance, to minimize the growth rate.

Within the scope of infinitesimal distortion, the change in the kinetic energy induced by parameter perturbations can be limited by a prescribed small energy modification $r_0^2$, which is written as follows:

$$J = \int_0^\infty \rho \sum_i \left[ (\widetilde{\boldsymbol{\mathcal{M}}}_i - \boldsymbol{\mathcal{M}}_i) \nabla_{\boldsymbol{\mathcal{M}}_i} \bar{u} \right]^2 dy - r_0^2 = 0, \tag{9}$$

where the over-tilde "$\sim$" denotes the optimal parameter. Subsequently, $J$ can be viewed as the constraint equation for the Lagrange-based optimization problem. In order to find the optimal parameter perturbation, define the Lagrangian as follows:

$$L = \sigma - (\boldsymbol{\varphi}^\dagger, \boldsymbol{\mathcal{L}}\boldsymbol{\varphi}) + \lambda_J J, \tag{10}$$

where $\lambda_J$ is the Lagrange multiplier. The objective turns to be calculating the stationary point of $L$. The partial derivations of the Lagrangian with respect to $\sigma$, $\boldsymbol{\varphi}$, $\boldsymbol{\varphi}^\dagger$ and $\lambda_J$ all yield 0,[19] while the quantities $\rho$ and $\boldsymbol{\mathcal{M}}_i$ are determined by the fixed initial state instead of the constraint curved surface described by Eq. (9). Thereupon, the rest differentiation is performed over each parameter $\widetilde{\boldsymbol{\mathcal{M}}}_i$ $(i = 1, 2, \dots)$. Recall that in Sec. II, the differentiation of the inner product term on the r.h.s. of Eq. (10) finally yields the sensitivity $\nabla^{\mathrm{e}}_{\boldsymbol{\mathcal{M}}_i}\sigma$. Therefore, according to Eqs. (9) and (10), the differentiation to each parameter $\boldsymbol{\mathcal{M}}_i$ is given by

$$\frac{\partial L}{\partial \widetilde{\boldsymbol{\mathcal{M}}}_i} \delta\boldsymbol{\mathcal{M}}_i = (\nabla^{\mathrm{e}}_{\boldsymbol{\mathcal{M}}_i}\sigma, \delta\boldsymbol{\mathcal{M}}_i) + 2\lambda_J \int_0^\infty \rho(\widetilde{\boldsymbol{\mathcal{M}}}_i - \boldsymbol{\mathcal{M}}_i) \times (\nabla_{\boldsymbol{\mathcal{M}}_i}\bar{u})^2 dy \delta\boldsymbol{\mathcal{M}}_i = 0. \tag{11}$$

Writing the term $\int_0^\infty \nabla^{\mathrm{e}}_{\boldsymbol{\mathcal{M}}_i}\sigma_r dy / \int_0^\infty \rho(\nabla_{\boldsymbol{\mathcal{M}}_i}\bar{u})^2 dy$ simply as $S_i$ and taking the real part of Eq. (11) give the optimal increment as follows:

$$\widetilde{\boldsymbol{\mathcal{M}}}_i - \boldsymbol{\mathcal{M}}_i = \pm S_i/(2\lambda_J). \tag{12}$$

The sign on the r.h.s. of Eq. (12) is undetermined since the sign before $J$ in Eqs. (9) and (10) is artificially appointed. Substituting Eq. (12) back into the constraint Eq. (9) gives the Lagrange multiplier where the positive sign is taken,

$$\lambda_J = \frac{1}{2r_0}\sqrt{\int_0^\infty \rho \sum_i (S_i \nabla_{\boldsymbol{\mathcal{M}}_i}\bar{u})^2 dy}. \tag{13}$$

Since the aim here is to minimize the growth rate, a negative sign on the r.h.s. of Eq. (12) should be taken so that the increment $\delta\boldsymbol{\mathcal{M}}_i$ and $\int_0^\infty \nabla^{\mathrm{e}}_{\boldsymbol{\mathcal{M}}_i}\sigma_r dy$ would have the opposite sign. Substituting Eq. (13) into Eq. (12), we obtain the final optimal increment of $\boldsymbol{\mathcal{M}}_i$ as follows:

$$\widetilde{\boldsymbol{\mathcal{M}}}_i - \boldsymbol{\mathcal{M}}_i = -r_0 S_i \Big/ \left( \sqrt{\int_0^\infty \rho \sum_i (S_i \nabla_{\boldsymbol{\mathcal{M}}_i}\bar{u})^2 dy} \right). \tag{14}$$

If the optimization objective is changed to maximize the integration of $\sigma_r$ in the propagation direction of disturbances (actually the amplified factor of the amplitude) in the $e^N$ method, the constraint Eq. (9) and the sensitivity in Eq. (14) should be in the corresponding integration form.

### B. Inverse design approach

The inverse design problem can be summarized as what combinations of increments in the control flow parameters should be superimposed on an original state if designers specify how the growth rate or $N$-factor varies at a given location. In the scenario of linear sensitivity, we assume that the goal of the inverse design problem is to delay the transition location, for example, the exit $Re_{max}$ of the

computational domain, by a minor percent $b\%$. In the $e^N$ method, $Re_{max}$ denotes the critical Reynolds number corresponding to a semi-empirical critical $N$-factor. Our purpose is to establish the equation that the perturbation of control parameters has to satisfy under the linear assumption. The known information is the $N \sim Re$ curve as well as the sensitivities obtained by the direct-adjoint LST.

First, the infinitesimal delay of $Re_{max}$ results in the decrease in $N$-factor at a certain location. The variation of the $N$-factor at $Re = Re_{max}$ arising from the parameter perturbation can be estimated by

$$\delta N = -\left.\frac{\partial N}{\partial Re}\right|_{Re=Re_{max}} \delta Re_{max}. \tag{15}$$

Substituting the objective $\delta Re_{max} = Re_{max} b\%$. into the equation above yields

$$\delta N = -\left.\frac{\partial N}{\partial Re}\right|_{Re=Re_{max}} Re_{max} b\%. \tag{16}$$

Meanwhile, $\delta N$ can be predicted by the integration of the spatial growth rate variation in the propagation direction of disturbances. By taking the two-dimensional disturbance propagated in the streamwise direction, for example, $\delta N$ can be calculated by[34]

$$\delta N = 2\int_{Re_{min}}^{Re_{max}} \delta\sigma_r dRe. \tag{17}$$

Substituting Eq. (4) into Eq. (17) and applying the trapezoidal rule in each discrete unit of $Re$ finally yield

$$\begin{aligned}\delta N &= 2\sum_i \int_{Re_{min}}^{Re_{max}} \int_0^\infty \nabla^e_{\mathcal{M}_i}\sigma_r dy \delta\mathcal{M}_i dRe \\ &\approx 2\sum_i \sum_{k=0}^{n-1}\left(\int_0^\infty \nabla^e_{\mathcal{M}_i}\sigma_r dy\right)_{k+1/2} \delta\mathcal{M}_i \Delta Re_k.\end{aligned} \tag{18}$$

Here, the subscript "$k+1/2$" represents the mean value of $k$th and $(k+1)$th discrete nodes, while $n$ is the total number of discrete streamwise intervals. With combination of Eqs. (16) and (18), the final constraint equation for the inverse design can be obtained. For the considered flow control problem, specify the parameter as $\mathcal{M} = (V_w, \beta_H)^{\mathrm{T}}$. Thus, the constraint equation is given by

$$A_1\delta V_w + A_2\delta\beta_H = -\partial N/\partial Re|_{Re=Re_{max}} Re_{max} b\%, \tag{19}$$

where $A_1$ and $A_2$ are coefficients related to $Re_{max}$ and streamwise and wall-normal integration of the sensitivity. Given the objective of inverse design, the parameter perturbation can therefore be figured out. Similar to the optimization approach, if the assumption of small parameter perturbation is disobeyed, iterative inverse design should be applied.

## IV. RESULTS

### A. Optimal states and associated mechanisms due to small parameter perturbations

The present focus point is the optimal parametric state and the contributions of various physical sources in the linear stability equation. As a beginning, the examination of the case of the infinitesimal parameter perturbation imposed on a typical initial state is presented.

Consider the parameter perturbation constraint Eq. (9) that limits the base flow kinetic energy change in a minor ratio, e.g., $r_0 = 1 \times 10^{-4}$, so that the BFD affects the eigenvalue linearly through the linear stability equation. Calculations of mode S in the supersonic flat-plate boundary layer are performed using the following settings: the edge Mach number $Ma_e = 4.5$, the wall conditions are no-slip for the base velocity and adiabatic for the base temperature, the Reynolds number $Re = 2000$. In addition, to satisfy the self-similarity condition,[25] the Prandtl number $Pr = 1$ and the dynamic viscosity are computed via the linear Chapman–Rubesin law where the dimensionless quantities satisfy $\mu = T$. As explained in Sec. II, parameters $V_w$ and $\beta_H$ are set to constants which are irrelevant to coordinates and satisfy the self-similarity condition. In this subsection, the dimensionless disturbance frequency is fixed at $F = 2\pi f^* \mu_e^*/(\rho_e^* U_e^{*2}) = 5 \times 10^{-5}$, where $f^*$ is the dimensional frequency of the mode.

In the established optimization and inverse design approaches, there is no additional requirement on the governing base flow and stability equations provided the concerned flow parameters appear explicitly. Thus, the two approaches are applicable to different regimes from subsonic to hypersonic flows, although the Mach 4.5 case is investigated in detail. Figure 1 shows the comparison of the homotopy analysis and shooting method on the base velocity and temperature profiles in the considered state, and good agreement is reached.

Figure 2 shows the calculated closed curve of the parameter pair $(V_w, \beta_H)$ that corresponds to the constraint Eq. (9). The original state is $(V_w, \beta_H) = (0, 0)$, where no pressure gradient or wall blowing or suction is imposed. To establish a one-to-one correspondence, the parametric angle $\theta$ that denotes the control state vector $(V_w, \beta_H)^{\mathrm{T}}$ on the constraint curve is introduced and marked in Fig. 2. For example, $\theta = 0$ indicates that the flow control state is wall suction in conjunction with zero pressure gradient. Figure 3(a) shows the results of $\delta\sigma_r$ shifting from the initial state $(V_w, \beta_H) = (0, 0)$ to the state point that travels along the constraint curve in Fig. 2 for a circle. The agreement of the solid line and the symbol, based on the direct LST and the parameter-associated sensitivity theory, respectively, demonstrates that the selected value of $r_0$ is consistent with the linearity assumption

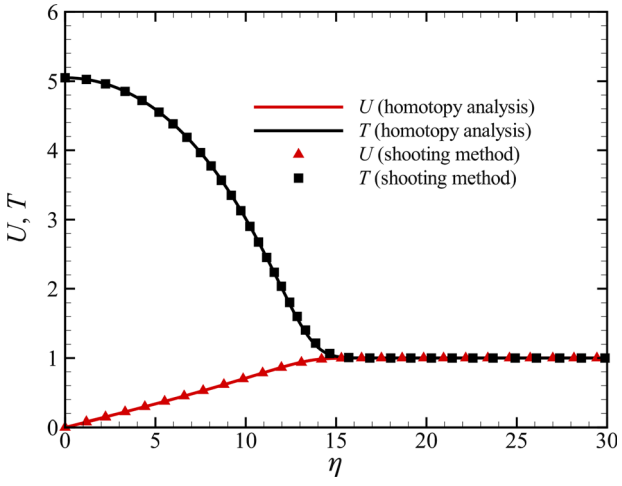


**FIG. 1.** Comparison of the base velocity and temperature profiles in the state $Ma_e = 4.5$ and $(V_w, \beta_H) = 0$ under adiabatic wall condition.

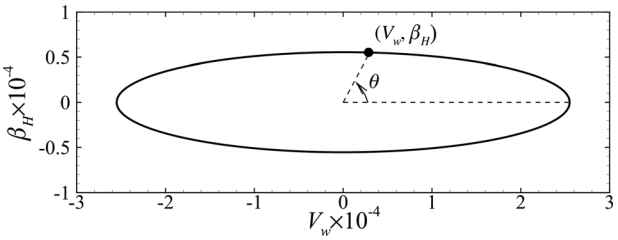


**FIG. 2.** The parametric curve corresponding to the base flow energy constraint equation (9) with $r_0 = 1 \times 10^{-4}$ and the definition of the parametric angle $\theta$ corresponding to the state $(V_w, \beta_H)$.

of the established sensitivity theory. Furthermore, the arrows that mark the most stable state ($\theta \approx 11.0°$, optimal state) and unstable state ($\theta \approx 191.0°$, the most dangerous state) via the Lagrangian approach in Sec. III A show a perfect agreement with the LST and sensitivity theory. Hence, the reliability of the established optimization theory is confirmed.

Note that the optimal state vector in Fig. 3(a) constrained by Eq. (9) is not equivalent to the gradient vector $(\partial\sigma_r/\partial V_w, \partial\sigma_r/\partial\beta_H)$. The gradient vector turns out to be optimal only if the constrained curve is a circle. In the shown case of energy-based constraint, the reported optimal state by LST, sensitivity theory, and the Lagrangian approach converges to $(V_w, \beta_H) = (1.9 \times 10^{-4}, 3.7 \times 10^{-5})$. Therefore, in this case, the combinations of favorable pressure gradient and relatively stronger steady suction lead to the most stable response of the local boundary layer. Another detected interesting aspect is named as the "invariant states" at $\theta = 166.4°$ and $\theta = 346.4°$, where $\delta\sigma_r = 0$ illustrated by Fig. 3(a). This indicates that along these two directions given by the $\theta$ value, the growth rate is invariant compared to the unperturbed base state at the origin. Coincidentally, the contributions of base velocity and temperature distortion are also observed to vanish simultaneously in the invariant states. The flow control parameter pair $(V_w, \beta_H) = (-1.7 \times 10^{-4}, 4.1 \times 10^{-5})$ or $(V_w, \beta_H) = (1.7 \times 10^{-4}, -4.1 \times 10^{-5})$ results in the invariant states, i.e., an appropriate combination of wall blowing and favorable pressure gradient or combination of wall suction and adverse pressure gradient.

As mentioned in Sec. II, the minor change of the parametric state only serves as a base flow modifier without any direct influence on the linear operator. Consequently, the response of the growth rate variation equals the first r.h.s. term of Eq. (6). This term can be simply decomposed into the separate contributions of $\delta U$ and $\delta T$, denoted as $\delta\sigma_{r,\delta U}$ and $\delta\sigma_{r,\delta T}$, which is the combined result of the velocity-related and temperature-related sensitivity in the Appendix, respectively. Figure 3(b) gives the characterization of both two BFD contributions that eliminate each other. Although a similar tendency has been observed by Park and Zaki[19] in a single state perturbation, extended calculations and confirmations are achieved in the optimization problem via the parameter-associated sensitivity theory. According to Fig. 3(b), the resulting total $\delta\sigma_r$ appears to be an order of magnitude smaller than each individual BFD contribution, and the sign of the total $\delta\sigma_r$ is found to synchronize with that of $\delta\sigma_{r,\delta U}$. In other words, the base velocity distortion finally determines whether the boundary layer grows more stable or unstable. The optimal state ($\theta \approx 11.0°$) appears with the presence of the largest superiority of $\delta\sigma_{r,\delta U}$ over $\delta\sigma_{r,\delta T}$. Coincidentally, the optimal state synchronizes the individual maximum of both the base velocity and temperature distortion.

To identify the dominator and grade the physical effects, the sources of the eigenvalue variation are categorized into eight types totally, containing the changes in the (1) mean shear production, (2) the advection, (3) the viscous dissipation, (4) the continuity equation, (5) the pressure gradient, (6) the base temperature gradient, (7) the thermal conduction, and (8) the pressure dilatation. The eight types are figured out by the contributions of the sensitivities in the Appendix orderly as $\nabla_U^1\sigma_r + \nabla_T^1\sigma_r$, $\nabla_U^2\sigma_r + \nabla_T^2\sigma_r$, $\nabla_U^3\sigma_r + \nabla_T^6\sigma_r$, $\nabla_T^3\sigma_r$, $\nabla_T^4\sigma_r$, $\nabla_T^5\sigma_r$, $\nabla_T^7\sigma_r$, and $\nabla_T^8\sigma_r$, respectively. The contributive magnitudes of all the physical effects are plotted in Fig. 4. The first-class physical effects appear to be the advection and mean shear, where the advection term is more significant in the range $0 \le \theta \le 360°$.

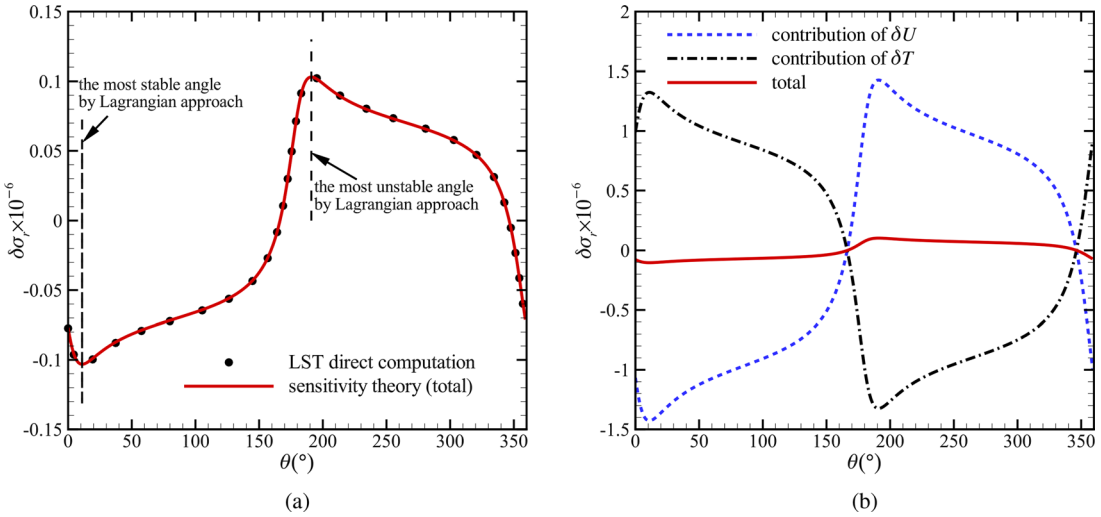


**FIG. 3.** Response of the growth rate variation to the change from $(V_w, \beta_H) = (0, 0)$ to the state $(V_w, \beta_H)$ with parametric angle $\theta$ on the energy constraint curve in Fig. 2: (a) total growth rate variation and (b) contributions of each BFD.

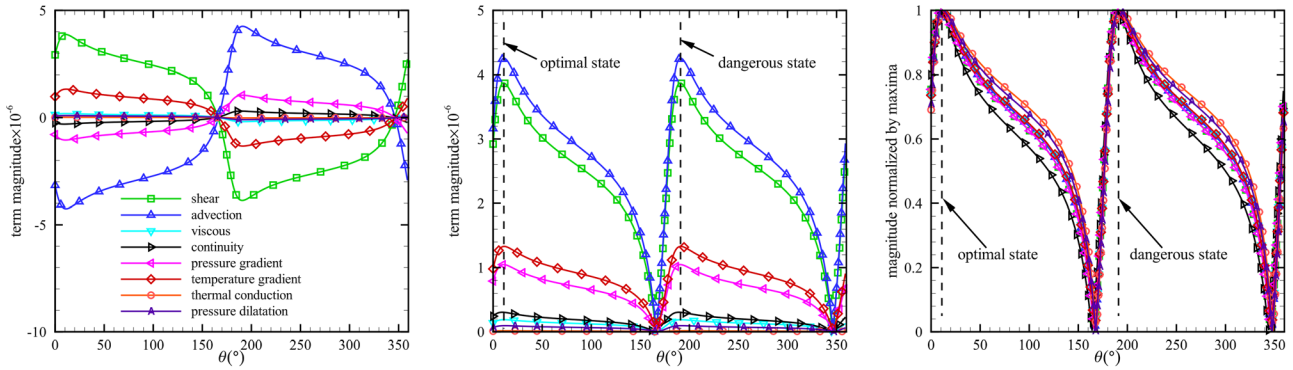


**FIG. 4.** Physical contributions to the growth rate variation due to the change from $(V_w, \beta_H) = (0, 0)$ to the state $(V_w, \beta_H)$ with parametric angle $\theta$ on the energy constraint curve in Fig. 2: (a) magnitude, (b) absolute value of the magnitude, and (c) absolute magnitude normalized by each maximum.

The second-class physical causes are the base temperature gradient and the pressure gradient terms, where the former is stronger. The remaining causes, including the pressure dilatation that is significant in the evolvement and sustainability of the second mode instability,[35] are regarded as minor effects in the local optimization problem. This can be attributed to the fact that these marginal terms are relatively insensitive to the BFD induced by the parameter perturbation. According to the term sign in Fig. 4(a), the growth rate variation can be viewed as the consequence of the entire contribution of $(|\delta\sigma_{r,\text{advection}}| - |\delta\sigma_{r,\text{shear}}|) + (|\delta\sigma_{r,\text{temperature gradient}}| - |\delta\sigma_{r,\text{pressure gradient}}|) + \text{minor}$ effects. The optimal state appears on the occasion that the major effects like $(|\delta\sigma_{r,\text{advection}}| - |\delta\sigma_{r,\text{shear}}|)$ contribute the most negatively to the growth rate increment.

Another noteworthy phenomenon is that all the physical effects reach each maximum synchronously in the vicinity of the optimal and dangerous states in Fig. 4(b). By normalization based on each maximum, Fig. 4(c) displays the synchronous behavior of the eight types of physical effects throughout the constraint curve in Fig. 2. Particularly, the $\delta\sigma_r \sim \theta$ curves of the four leading effects collapse into one curve. Therefore, with an invariant base-flow kinetic energy change, the four major effects behave similarly with varying input parameter perturbations.

## B. Optimal states and associated mechanisms due to finite parameter perturbations

### 1. Gradient field and optimal states

Section IV A provides fundamental knowledge to the roles of physical terms in the linear stability equation when the parameter perturbation is small. An extensive examination of the finite parameter perturbation is necessary for further practical applications. Consider a finite square parameter domain: $-0.3 \le V_w, \beta_H \le 0.3$. A straightforward way to investigate the parametric influence inside the box $-0.3 \le V_w, \beta_H \le 0.3$ is to plot the pathline of the gradient vector $(\partial\sigma_r/\partial V_w, \partial\sigma_r/\partial\beta_H)$ calculated by Eq. (6). Moving toward the direction of the gradient vector leads to the most rapid increase in the growth rate, while upstream of the pathline indicates a more stable state.

Before selecting a fixed disturbance frequency to observe the gradient field, we first examine the effect of control parameters, say $\beta_H$, on the broadband mode S. As a reference, Zurigat *et al.*[36] presented the effect of pressure gradient by solving the non-similar boundary layer equation and the compressible linear stability equation. Consistent with the approach of Zurigat *et al.*, the edge Mach number at the concerned location is held fixed while the parameter $\beta_H$ varies from negative to positive values. Meanwhile, no steady wall blowing or suction is imposed such that $V_w = 0$.

Figure 5 shows the effect of $\beta_H$ on the $\sigma_r \sim F$ curves. The reported tendency that increasing $\beta_H$, i.e., stronger favorable pressure gradient, reduces the peak growth rate and increases the most unstable frequency qualitatively agrees with the observation of Zurigat *et al.* This is consistent with the common knowledge that favorable pressure gradient stabilizes the first and second modes, since the eventual envelop curve for the $e^N$ method would move downward due to the

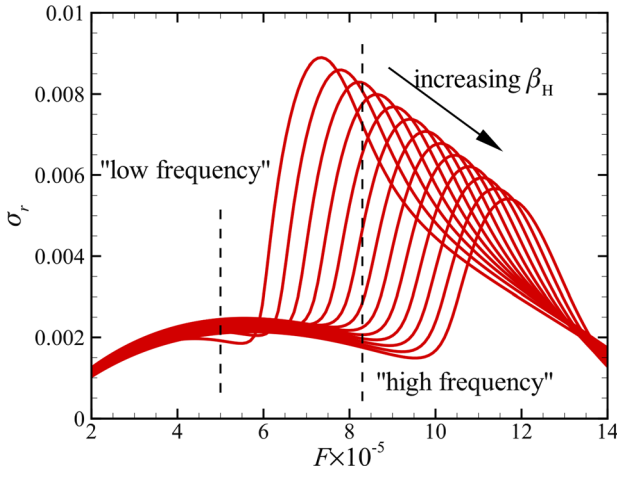


**FIG. 5.** Change of the mode S growth rate with the dimensionless frequency $F$ under the fixed $Ma_e = 4.5$ and $V_w = 0$ and increasing $\beta_H$ ranging from $-0.15$ and 0.15, where the spacing $\delta\beta_H = 0.025$. The dash lines with the labels low frequency and high frequency denote $F = 5 \times 10^{-5}$ and $F = 8.3 \times 10^{-5}$, respectively.

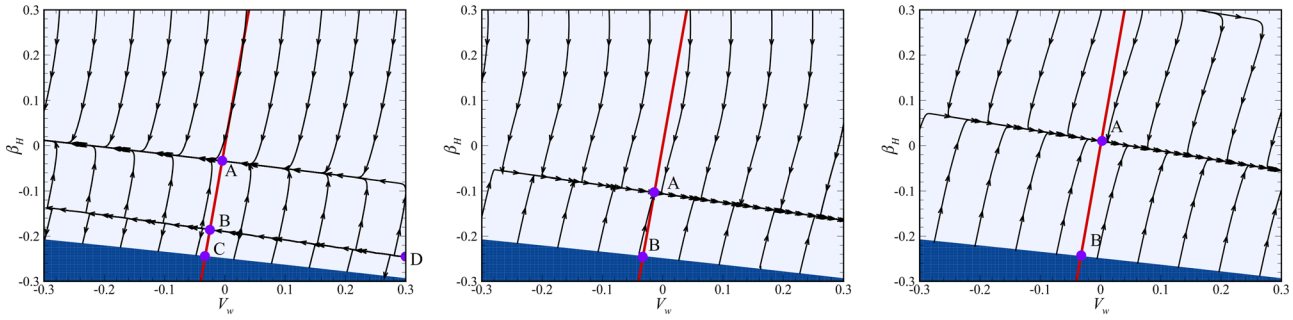


**FIG. 6.** Pathlines of the gradient field $(\partial\sigma_r/\partial V_w, \partial\sigma\alpha_r/\partial\beta_H)$ for (a) $Ma_e = 4.5$, low frequency, (b) $Ma_e = 4.5$, high frequency, and (c) $Ma_e = 6.5$, low frequency. The red line segment $\overline{AB}$ and the dark blue region represent the parametric ranges of the unusual physical effects of $(\delta V_w, \delta\beta_H)$ and the occurrence of the boundary layer separation, respectively.

decreased peak growth rate in Fig. 5. However, as also displayed by Zurigat *et al.*, favorable pressure gradient may sometimes destabilize the mode if the frequency is fixed, although the tendency of Zurigat *et al.* is weaker than the present one due partly to base flow differences. In the vicinity of the marked "high frequency" in Fig. 5, the growth rate first increases and then decreases with the growing $\beta_H$. The treatment of fixing the disturbance frequency can be regarded as a simulation of a single-frequency actuator that initiates the boundary layer transition experimentally. For a crucial single-frequency instability wave, the unusual nonmonotonous effect of the pressure gradient is of particular interest. Hereupon, two-dimensionless frequencies of $F = 5 \times 10^{-5}$ and $F = 8.3 \times 10^{-5}$, denoted as the "low frequency" and high frequency in Fig. 5, respectively, are chosen to investigate the nonmonotonous relationship. Both two frequencies are located in the unstable region of mode S, which actually correspond to the traditional first and second modes, respectively. Meanwhile, another case of Mach number 6.5 is also calculated.

Figure 6 shows the pathline plots of the concerned gradient vector for three different combinations of frequency and Mach number. The dark region represents the parametric range of the occurrence of boundary layer separation owing to a large adverse pressure gradient or wall blowing. The red solid line $\beta_H = 7.5V_w$, approximately perpendicular to the interface lines of pathlines with different vector directions, are highlighted for convenient description. Clearly, all the three subfigures illustrate an unusual behavior on the line segment $\overline{AB}$, where the vector $(\partial\sigma_r/\partial V_w, \partial\sigma_r/\partial\beta_H)$ points to the positive directions of the $V_w$ and $\beta_H$ axes. That means, between the A and B state points, enhanced favorable pressure gradient and steady wall suction results in the destabilization of the mode S. Subsequent sensitivity-based decomposition of the gradient $(\partial\sigma_r/\partial V_w, \partial\sigma_r/\partial\beta_H)$ should be beneficial to clarify the source of the mentioned performance. The detailed parameter values for the labeled states in Figs. 6–8 are given in Table I.

Prior to the gradient decomposition analysis, the global optimal state could be confirmed not to be located inside the domain $-0.3 < V_w, \beta_H < 0.3$, since no twist of the pathline is found that forms an interior stationary point. It is therefore inferred that the optimal state in the attached flow region is located around the borderline of the domain. Having examined both the interior and borderline regions of the box $-0.3 < V_w, \beta_H < 0.3$, it is found that the most stable state in

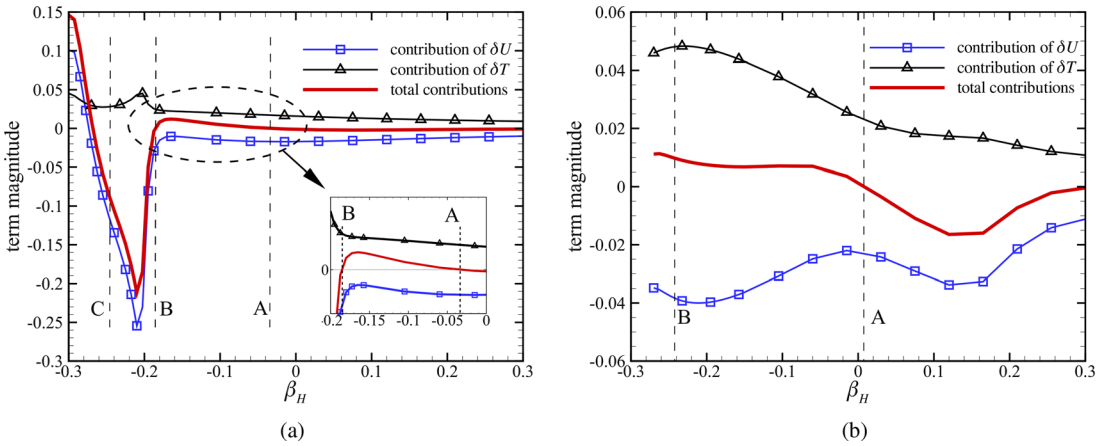


**FIG. 7.** The variation of $\partial\sigma_r/\partial\beta_H$ and the contributive components of the BFDs $\delta U$ and $\delta T$ for (a) $Ma_e = 4.5$, low frequency and (b) $Ma_e = 6.5$, low frequency, along $\beta_H = 7.5V_w$, i.e., the red solid line in Fig. 6(a) or 6(c). The vertical dashed lines with labels "A, B, C" correspond to the states "A, B, C" in Fig. 6, respectively.

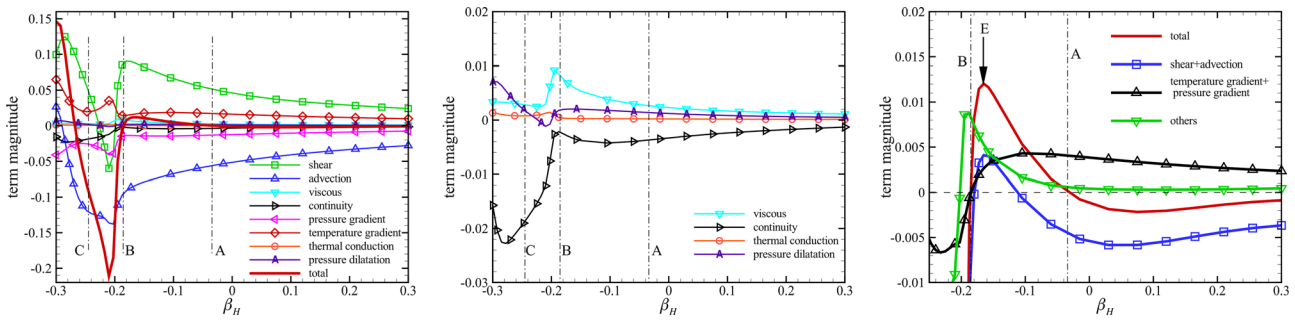


**FIG. 8.** The contributions of physical terms in the stability equation to $\partial\sigma_r/\partial\beta_H$ for (a) all physical terms, (b) minor terms, and (c) combinations of leading terms and others, along $\beta_H = 7.5V_w$ at "$Ma_e = 4.5$, low frequency," i.e., the red solid line in Fig. 6(a). The vertical dashed dotted lines with labels "A, B, C" correspond to the states "A, B, C" in Fig. 6, respectively.

Fig. 6(a) is state D on the borderline with an adverse pressure gradient and steady wall suction. This result seems sensible because the state D is exactly at upstream of one pathline of the gradient field. Nevertheless, suggested by Fig. 5, if the frequency is broadband, the optimal state is considered as the combination of the strongest favorable pressure gradient and wall suction that is consistent with the previous knowledge. Another extension from Sec. IV A is that the aforementioned invariant states should be the countless state trajectories which are perpendicular to the gradient pathline. Parameter pair varying along these trajectories would not contribute to the eigenvalue change.

### 2. Contributions of physical terms to the gradient field

For further investigations, the gradient $\partial\sigma_r/\partial\beta_H$ is decomposed into the contributions of either the base flow distortion $\delta U$ and $\delta T$ or the aforementioned eight physical effects. The discussion of $\partial\sigma_r/\partial\beta_H$ is representative since the sign of $\partial\sigma_r/\partial V_w$ is seen to change synchronously with $\partial\sigma_r/\partial\beta_H$. Tracking along the observed line $\beta_H = 7.5V_w$, the individual contribution of each BFD to $\partial\sigma_r/\partial\beta_H$ and the sum are jointly shown in Fig. 7 for Mach numbers 4.5 and 6.5 at the low frequency. For both cases, the final sign of $\partial\sigma_r/\partial\beta_H$ is entirely determined by the base velocity distortion, which resembles the finding in Sec. IV A. What differs is that the contribution of $\delta T$ exceeds that of $\delta U$ in the intermediate state between A and B. This unexpected phenomenon occurs accompanied by a combination of adverse pressure gradient and either wall blowing or suction.

From another perspective, it can be predicted that the positive contributions from the main physical effects to the gradient $\partial\sigma_r/\partial\beta_H$ are promoted between the states A and B. As an example, Figs. 8(a)–8(c) provide the budgets of all the physical effects, the minor terms and the combined effects for the Mach 4.5 low frequency case, respectively. Generally, the degree of importance of the eight physical effects is identical to the case for the infinitesimal parameter perturbation. The exceptional situation is observed in the range $\beta_H < \beta_{H,\text{state B}}$, where the minor effects become comparable to the major ones. In that exceptional range, the adverse pressure gradient is strong and the base flow has been heavily distorted compared to the zero-pressure-gradient state.

With respect to the unusuality between the states A and B, Fig. 8(c) illustrates that the contributions of (shear+advection), (temperature gradient+pressure gradient) and the minor effects are simultaneously promoted. What is uncommon in this parametric range is that the minor effects can even be comparable to the major ones. Figure 8(b) further shows the rise in the positive contribution of the minor effects is mainly attributed to the viscous dissipation. In terms of the major effects, it is interesting to discuss the characteristics of the significant sensitivity profiles in order to clarify how the perturbations of flow control parameters are conveyed through the governing equation and eventually contribute to the eigenvalue variation. Particularly, the mean shear contributes to the gradual production of disturbance energy. Furthermore, one interesting property is that the sensitivity profile $\nabla_U^1\sigma_r$ itself, arising from mean shear, contributes nothing to the eigenvalue change. The proof is that

$$\int_0^\infty \nabla_U^1\sigma_r dy = -\int_0^\infty \frac{d}{dy}\left(\frac{Re}{\mu T}\hat{u}^\dagger\hat{v}^{\mathrm{H}}\right)dy = -\left(\frac{Re}{\mu T}\hat{u}^\dagger\hat{v}^{\mathrm{H}}\right)\Big|_0^\infty = 0, \tag{20}$$

due to the vanished direct and adjoint eigenvectors imposed by the boundary conditions. However, the mean shear distortion actually

**TABLE I.** Detailed control parameters for the labeled states from A to E in Figs. 6–8.

| | $V_w$ | | | | | $\beta_H$ | | | | |
|---|---|---|---|---|---|---|---|---|---|---|
| | A | B | C | D | E | A | B | C | D | E |
| $Ma_e = 4.5$, low frequency | −0.0043 | −0.025 | −0.033 | 0.3 | −0.022 | −0.034 | −0.19 | −0.24 | −0.25 | −0.17 |
| $Ma_e = 4.5$, high frequency | −0.014 | −0.033 | ⋯ | ⋯ | ⋯ | −0.10 | −0.25 | ⋯ | ⋯ | ⋯ |
| $Ma_e = 6.5$, low frequency | 0.001 | −0.032 | ⋯ | ⋯ | ⋯ | 0.01 | −0.24 | ⋯ | ⋯ | ⋯ |

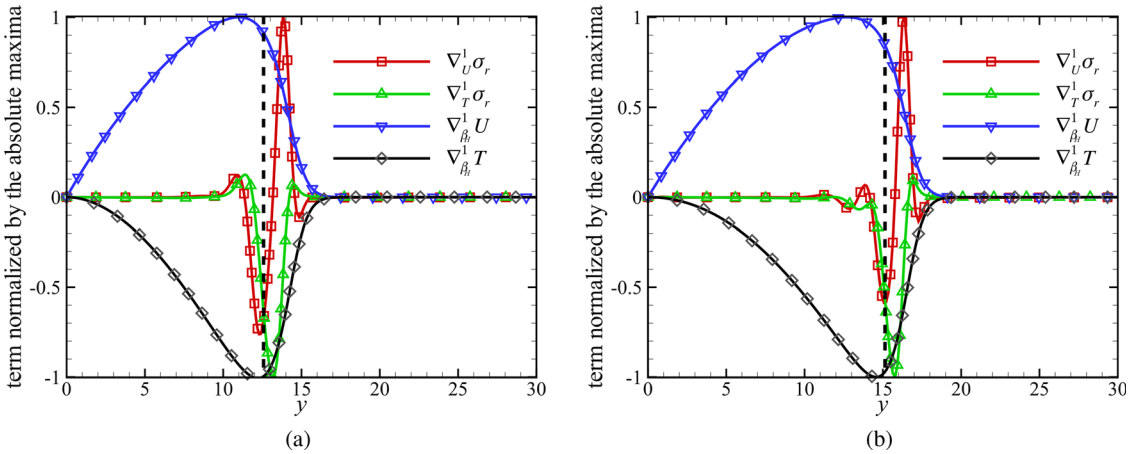


**FIG. 9.** The sensitivity profiles related to mean shear normalized by each maximal absolute value in the state "$Ma_\theta = 4.5$, low frequency" for (a) state A and (b) state E. The vertical dashed line denotes the critical layer location. The states A and E are marked in Fig. 8(c).

generates the eigenvalue variation according to Fig. 8(a). The key point here is that the base velocity distortion $\delta U$ determined by the parameter perturbation acts as a role of modulator that alters the final contribution of the mean shear, formulated as $\delta\sigma_r = \int_0^\infty \nabla_U^1\sigma_r \delta U dy \neq 0$. The base velocity distortion $\delta U$ is distributed ununiformly in the boundary layer and yields a nonzero response of $\delta\sigma_r$. Further evidence is subsequently shown on the behavior of the mean shear sensitivity profile.

Two representative states are chosen for the discussion of the contribution of mean shear, namely, state A that records the sign change of the gradient $\partial\sigma_r/\partial\beta_H$ and state E in Fig. 8(c) that has the maximal positive gradient $\partial\sigma_r/\partial\beta_H$. Figure 9 shows four significant sensitivity profiles related to mean shear for both states A and E. The plotted sensitivity profiles are crucial since the response arising from mean shear is given by the information transfer equation according to Eq. (6),

$$\delta\sigma_r^1 = \left(\nabla_{V_w} U\nabla_U^1\sigma_r, \delta V_w\right) + \left(\nabla_{V_w} T\nabla_T^1\sigma_r, \delta V_w\right) + \left(\nabla_{\beta_H} U\nabla_U^1\sigma_r, \delta\beta_H\right) + \left(\nabla_{\beta_H} T\nabla_T^1\sigma_r, \delta\beta_H\right). \quad (21)$$

The four profiles $\nabla_{V_w} U$, $\nabla_{V_w} T$, $\nabla_{\beta_H} U$, and $\nabla_{\beta_H} T$ are entirely determined by the base flow equation, while the remaining two $\nabla_U^1\sigma_r$ and $\nabla_T^1\sigma_r$ are related to the stability equation. According to Figs. 8(a) and 8(b), both $\nabla_U^1\sigma_r$ and $\nabla_T^1\sigma_r$ are located in negative valleys in the vicinity of the critical layer (dashed lines). This feature is consistent with our previous conclusion.[25] Although a positive peak of the profile $\nabla_U^1\sigma_r$ is found above the critical layer, the base-flow-related profile $\nabla_{\beta_H} U$ is positively larger in the vicinity of the negative valley of $\nabla_U^1\sigma_r$. Therefore, as indicated by Eq. (21), a positive distortion $\delta\beta_H$ gives rise to a negative response of $\delta\sigma_r$ through velocity-related product $\nabla_{\beta_H} U\nabla_U^1\sigma_r$ in the mean shear mechanism. This is true in the incompressible flow stability problem. However, it is inconsistent with the observation in Fig. 8(a) that mean shear contributes to a positive $\partial\sigma_r/\partial\beta_H$. The difference is attributed to the nonzero $\delta T$ in compressible flows. Figure 9 shows that the sensitivity $\nabla_T^1\sigma_r$ normalized by its maximum owns a dominant valley and no major peaks, and that $\nabla_{\beta_H} T$ and $\nabla_T^1\sigma_r$ have the same sign. That suggests the temperature distortion through $\nabla_{\beta_H} T\nabla_T^1\sigma_r$ yields a larger positive response of $\delta\sigma_r$ than the negative response by velocity-related part $\nabla_{\beta_H} U\nabla_U^1\sigma_r$ in Eq. (21).

To provide exact evidence, the original magnitude without normalization is shown in Fig. 10. It is illustrated that the temperature-related product $\nabla_{\beta_H} T\nabla_T^1\sigma_r$ in Eq. (21) has a remarkable peak. In contrast, the velocity-related product $\nabla_{\beta_H} U\nabla_U^1\sigma_r$ owns multiple peaks and valleys that eliminate each other during the $y$-directional integration from the wall to infinity. It can be predicted that the positive temperature-related contribution to the gradient $\partial\sigma_r/\partial\beta_H$ exceeds that of the velocity-related part. Eventually, the mean-shear-induced growth rate variation is positive for both states A and E, which agrees

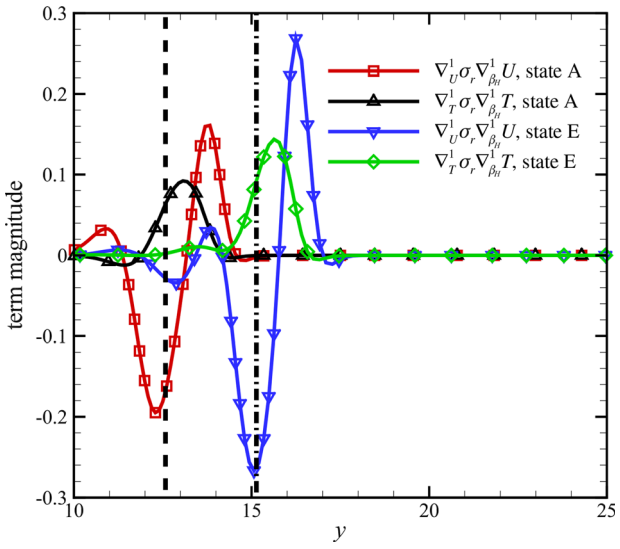


**FIG. 10.** The contributions of mean shear distortion including parts of $\delta U$ and $\delta T$ to $\partial\sigma_r/\partial\beta_H$ in the state "$Ma_\theta = 4.5$, low frequency." The vertical dashed and dashed dotted lines denote the critical layer locations of the states A and E, respectively, which are marked in Fig. 8(c).

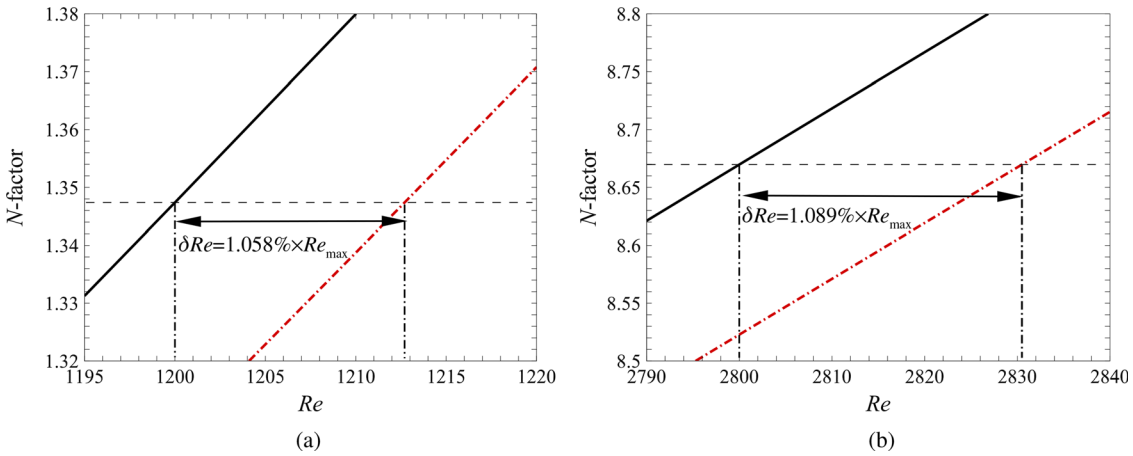


**FIG. 11.** The $N \sim Re$ curves of the initial state (solid line) and state after the inverse design (dash dotted line) with the initial state $Ma_e = 4.5$ and $V_w = \beta_H = 0.005$ for the object (a) $Re_{max} = 1200$, $b = 1$ and (b) $Re_{max} = 2800$, $b = 1$.

with the distribution in Fig. 8(a). The theoretical calculation also confirms that the temperature-related contribution to the gradient $\partial\sigma_r/\partial\beta_H$ is around twice of the velocity-related counterpart in the mean shear mechanism. Please note that the analysis is independent of the magnitude of the external control parameter perturbation. Therefore, the aforementioned modulator role of the $\delta U$ and the finally determined sign of $\partial\sigma_r/\partial\beta_H$ are intrinsic properties of the linear system in the considered states.

### C. Parametric inverse design

Based on the inverse design formulation in Sec. III, as long as the minor perturbations of the flow control parameters satisfy Eq. (19), the target of $b$% delay of $Re_{max}$ would be achieved. To verify the established inverse design method, two perturbations $(\delta V_w, \delta\beta_H) = (0.132, 0)$ and $(\delta V_w, \delta\beta_H) = (0.121, 0)$ are selected, which satisfy Eq. (19) for the targets $Re_{max} = 1200$, $b = 1$ and $Re_{max} = 2800$, $b = 1$, respectively. Physically, the two control parameter perturbations represent different strength of steady wall suction. The perturbation of $\beta_H$ is also alternative to achieve the inverse design goal. Subsequently, the chosen parameter perturbations are superimposed on the initial state to obtain an updated $N$-factor curve. The original and perturbed $N \sim Re$ curves for mode S are compared in Figs. 11(a) and 11(b). The actual effect of the inverse design is to delay the $Re_{max}$ by 1.058% with an invariable critical $N$ for the case $Re_{max} = 1200$, $b = 1$, while the percentage is 1.089% for the target $Re_{max} = 2800$, $b = 1$. The outcome approaches the goal of delaying by 1%.

In terms of larger finite modifications to parameters, iterative inverse design is necessary. An iterative inverse design procedure for a finite magnitude of goal parameter $b_d$ is proposed with the flow chart given in Fig. 12. Basically, the goal of delaying the transition location by $b_d$% is achieved by dividing $b_d$% into a sequence of minor $b_n$% in order to satisfy the linearity assumption of the inverse design formulation. This general procedure allows for the adoption of base flow solutions in self-similar, non-similar or computation fluid dynamics (CFD) types. By utilizing the established method, the accumulated parameter perturbations give a final theoretical prediction of to what degree the flow control strategies should be adjusted in order to achieve the desired variation of the transition location.

Figure 13 shows the examination of the parametric inverse design with and without iterative procedures under the finite $b$. Here, the solid line represents the accurate limit of the inverse design, where the delay percentage of $Re_{max}$ exactly equals the desired goal. The adjusted parameter in this case is $V_w$, while $\beta_H$ is fixed at 0. The result without the iterative procedure is shown to deviate from the goal gradually.

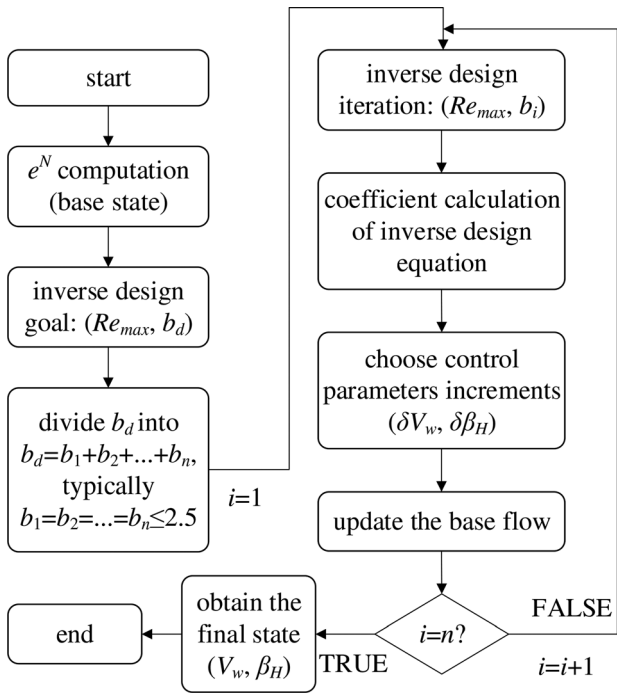


**FIG. 12.** The general inverse design procedure with a finite goal parameter $b_d$.

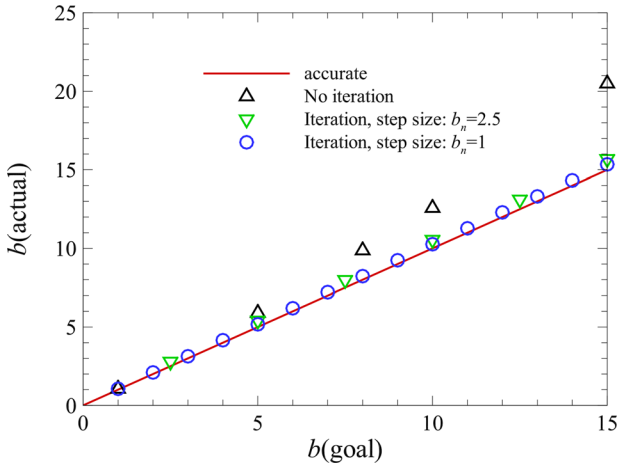


**FIG. 13.** The actual $b$, i.e., delay percentage of $Re_{max} = 1200$, vs the finite goal parameter $b$. The solid line denotes the exact limit of the inverse design. Initial state is identical to that of Fig. 11.

In contrast, iterative procedures with two different step sizes demonstrate a good agreement with the exact limit. For example, if the goal is to delay the $Re_{max}$ by 10%, three cases including the method without iterative procedures, the method with the iterative step size $b_n = 2.5$ and one with the step size $b_n = 1$ are found to delay $Re_{max}$ by about 12.58%, 10.55%, and 10.27%, respectively. The corresponding perturbations of the blowing-suction parameter $\delta V_w$ are 1.32, 1.13, and 1.10, respectively. In summary, the inverse design approach is verified to be effective for the parametric estimation, and the iterative manner improves the accuracy for a large shift of the critical Reynolds number.

## V. CONCLUSION

Based on the previously established parameter-associated sensitivity expression and the method of Lagrange multipliers, the present work analytically derives the optimal parameter perturbation under a certain constraint of the change in the base flow kinetic energy. The optimal state is considered to minimize the growth rate of the local boundary layer disturbance. In addition, within the framework of the $e^N$ method, the equation of parameter perturbations is derived for the inverse design. Specifically, the control parameters steady blowing-suction factor $V_w$ and the generalized Hartree parameter $\beta_H$ are investigated mainly at Mach number 4.5.

Excellent agreement between the direct LST calculation, sensitivity theory, and Lagrangian approach is achieved for the optimal parametric state due to minor parameter perturbations. The sign of the growth rate variation synchronizes the contributive part of the base velocity distortion. The optimal state occurs if the base velocity distortion has the greatest advantage over that of the temperature. Furthermore, contributions of various physical sources to the growth rate behave similarly and collapse onto one curve, particularly for the major four: advection, mean shear, base temperature gradient, and pressure gradient.

In terms of the finite parameter perturbation, the optimal state is found on the constraint border of $V_w$ and $\beta_H$. Although the favorable pressure gradient and wall suction stabilize the broadband mode S, an opposite tendency may be observed for a single-frequency disturbance. In this unusual range, positive contributions of both the major and minor physical effects to the growth rate are promoted. The contributive increase in major and minor effects are attributed to the enhancement of mean shear and viscous effect, respectively. Based on the decomposition analysis, the sign of the gradient $\partial\sigma_r/\partial\beta_H$ is intrinsically determined by the effective sensitivities, which is irrelevant to the parameter perturbation magnitude.

Finally, the inverse design method is verified within tolerance. Given the minor variation in the critical Reynolds number, the required equation of the input control parameter perturbation is inversely obtained. For the finite perturbation, an iterative procedure is proposed to achieve the inverse design goal and verified. In the future work, non-parallel flow stability analysis can be further considered in the parameter design.

## ACKNOWLEDGMENTS

This research is supported by the National Natural Science Foundation of China through Grant No. 11872094, the National Defense Foundation Enhancement Program through Grant No. 2019JCJQJJ245 and the Research Grants Council, Hong Kong, under Contract No. 15216621.

## AUTHOR DECLARATIONS

### Conflict of Interest

The authors have no conflicts to disclose.

### Author Contributions

**Peixu Guo:** Conceptualization (lead); Formal analysis (lead); Investigation (lead); Methodology (lead); Resources (equal); Software (lead); Validation (lead); Writing – original draft (lead); Writing – review & editing (lead). **Fangcheng Shi:** Methodology (supporting); Writing – review & editing (supporting). **Zhenxun Gao:** Funding acquisition (equal); Resources (equal); Supervision (equal); Writing – review & editing (supporting). **Chongwen Jiang:** Writing – review & editing (supporting). **Chun-Hian Lee:** Supervision (equal); Writing – review & editing (supporting). **Chih-Yung Wen:** Formal analysis (supporting); Funding acquisition (equal); Supervision (equal); Writing – review & editing (supporting).

## DATA AVAILABILITY

The data that support the findings of this study are available from the corresponding author upon reasonable request.

## APPENDIX: LINEAR STABILITY EQUATION AND EXPRESSIONS OF THE STABILITY-RELATED SENSITIVITIES

Assume the base flow is two-dimensional (spanwise velocity $W = 0$) for the most unstable mode S ($\beta = 0$). The $x$- and $y$-directional momentum equations, the continuity equation, and the energy equation for LST in the Cartesian coordinate system are orderly given by

$$\frac{d^2\hat{u}}{dy^2}-\left(Re\frac{\sigma U-\mathrm{i}\omega}{\mu T}-l_2\sigma^2\right)\hat{u}-\left(Re\frac{dU}{dy}\frac{1}{\mu T}-\sigma\frac{1}{\mu}\frac{d\mu}{dT}\frac{dT}{dy}\right)\hat{v}$$
$$-\sigma\frac{Re}{\mu}\hat{p}+\left(\frac{1}{\mu}\frac{d\mu}{dT}\frac{d^2U}{dy^2}+\frac{1}{\mu}\frac{d^2\mu}{dT^2}\frac{dT}{dy}\frac{dU}{dy}\right)\hat{T}+\frac{1}{\mu}\frac{d\mu}{dT}\frac{dT}{dy}\frac{d\hat{u}}{dy}$$
$$+\sigma l_1\frac{d\hat{v}}{dy}+\frac{1}{\mu}\frac{d\mu}{dT}\frac{dU}{dy}\frac{d\hat{T}}{dy}=0, \tag{A1}$$

$$\frac{d^2\hat{v}}{dy^2}+\sigma\frac{l_1}{l_2}\frac{d\hat{u}}{dy}+\frac{1}{\mu}\frac{d\mu}{dT}\frac{dT}{dy}\frac{d\hat{v}}{dy}-\frac{Re}{l_2\mu}\frac{d\hat{p}}{dy}+\sigma\frac{l_0}{l_2}\frac{1}{\mu}\frac{d\mu}{dT}\frac{dT}{dy}\hat{u}$$
$$-\frac{1}{l_2}\left(Re\frac{\sigma U-\mathrm{i}\omega}{\mu T}-\sigma^2\right)\hat{v}+\sigma\frac{1}{l_2\mu}\frac{d\mu}{dT}\frac{dU}{dy}\hat{T}=0, \tag{A2}$$

$$\frac{d\hat{v}}{dy}+\sigma\hat{u}-\frac{1}{T}\frac{dT}{dy}\hat{v}+\gamma Ma^2(\sigma U-\mathrm{i}\omega)\hat{p}-\frac{\sigma U-\mathrm{i}\omega}{T}\hat{T}=0, \tag{A3}$$

$$\frac{d^2\hat{T}}{dy^2}+2(\gamma-1)PrMa^2\frac{dU}{dy}\frac{d\hat{u}}{dy}+\frac{2}{\mu}\frac{d\mu}{dT}\frac{dT}{dy}\frac{d\hat{T}}{dy}$$
$$+\left[2\sigma(\gamma-1)PrMa^2\frac{dU}{dy}-PrRe\frac{dT}{dy}\frac{1}{\gamma\mu T}\right]\hat{v}$$
$$-\frac{(\gamma-1)}{\gamma\mu}PrRe\left(\sigma\hat{u}+\frac{d\hat{v}}{dy}\right)+\left[-RePr(\sigma U-\mathrm{i}\omega)\frac{1}{\gamma\mu T}\right.$$
$$\left.+\sigma^2+(\gamma-1)PrMa^2\frac{1}{\mu}\frac{d\mu}{dT}\left(\frac{dU}{dy}\right)^2+\frac{1}{\mu}\frac{d^2\mu}{dy^2}\right]\hat{T}=0. \tag{A4}$$

Here, $l_j=j+\lambda/\mu$, and $\gamma$ and $\lambda$ denote the specific heat ratio and the second viscosity, respectively. To give the sensitivity expression, the variable $\hat{R}$ in Eq. (6) can be computed by $\hat{R}=\int_0^\infty \hat{R}_y dy$, where

$$\hat{R}_y=\hat{u}^{\dagger\mathrm{H}}\left[-\left(\frac{ReU}{\mu T}-2l_2\sigma\right)\hat{u}+\frac{1}{\mu}\frac{d\mu}{dT}\frac{dT}{dy}\hat{v}-\frac{Re}{\mu}\hat{p}+l_1\frac{d\hat{v}}{dy}\right]$$
$$+v^{\dagger\mathrm{H}}\left[\frac{l_1}{l_2}\frac{d\hat{u}}{dy}+\frac{l_0}{l_2}\frac{1}{\mu}\frac{d\mu}{dT}\frac{dT}{dy}\hat{u}-\frac{1}{l_2}\left(\frac{ReU}{\mu T}-2\sigma\right)\hat{v}\right.$$
$$\left.+\frac{1}{l_2}\frac{1}{\mu}\frac{d\mu}{dT}\frac{dU}{dy}\hat{T}\right]+p^{\dagger\mathrm{H}}\left[\hat{u}+\gamma Ma^2U\hat{p}-\frac{U}{T}\hat{T}\right]$$
$$+T^{\dagger\mathrm{H}}\left[2(\gamma-1)PrMa^2\frac{dU}{dy}\hat{v}-\frac{\gamma-1}{\gamma\mu}PrRe\hat{u}\right.$$
$$\left.-\left(\frac{PrReU}{\gamma\mu T}-2\sigma\right)\hat{T}\right]. \tag{A5}$$

In terms of the velocity-related sensitivity, the change in the mean shear term in the momentum equation generates

$$\nabla_U^1\sigma=-\frac{d}{dy}\left(\frac{Re}{\mu T}\hat{u}^\dagger\hat{v}^{\mathrm{H}}\right). \tag{A6}$$

The variation in the advection terms yields

$$\nabla_U^2\sigma=\frac{\sigma^{\mathrm{H}}Re}{\mu T}\left(\hat{u}^\dagger\hat{u}^{\mathrm{H}}+\frac{1}{l_2}\hat{v}^\dagger\hat{v}^{\mathrm{H}}+\frac{Pr}{\gamma}\hat{T}^\dagger\hat{T}^{\mathrm{H}}\right)$$
$$-\hat{p}^\dagger\left(\gamma Ma^2\sigma^{\mathrm{H}}\hat{p}^{\mathrm{H}}-\frac{\sigma^{\mathrm{H}}}{T}\hat{T}^{\mathrm{H}}\right). \tag{A7}$$

The distortion of the viscous stress and dissipation terms gives rise to

$$\nabla_U^3\sigma=\frac{d}{dy}\left\{-\frac{1}{\mu}\frac{d\mu}{dT}\frac{d\hat{u}^\dagger}{dy}\hat{T}^{\mathrm{H}}+\frac{1}{\mu^2}\left(\frac{d\mu}{dT}\right)^2\frac{dT}{dy}\hat{u}^\dagger\hat{T}^{\mathrm{H}}\right.$$
$$+\frac{\sigma^{\mathrm{H}}}{l_2\mu}\frac{d\mu}{dT}\hat{v}^\dagger\hat{T}^{\mathrm{H}}+2(\gamma-1)PrMa^2\hat{T}^\dagger\left(\frac{d\hat{u}^{\mathrm{H}}}{dy}\right.$$
$$\left.\left.+\sigma^{\mathrm{H}}\hat{v}^{\mathrm{H}}+\frac{1}{\mu}\frac{d\mu}{dT}\frac{dU}{dy}\hat{T}^{\mathrm{H}}\right)\right\}. \tag{A8}$$

In terms of the temperature-related sensitivity, the distortion of the mean shear term in the momentum equation leads to

$$\nabla_T^1\sigma=-\frac{Re}{(\mu T)^2}\frac{dU}{dy}\left(\mu+\frac{d\mu}{dT}T\right)\hat{u}^\dagger\hat{v}^{\mathrm{H}}. \tag{A9}$$

The distortion of the advection terms results in

$$\nabla_T^2\sigma=-\frac{Re}{(\mu T)^2}(\sigma^{\mathrm{H}}U+\mathrm{i}\omega)\left(\mu+\frac{d\mu}{dT}T\right)$$
$$\times\left(\hat{u}^\dagger\hat{u}^{\mathrm{H}}+\frac{1}{l_2}\hat{v}^\dagger\hat{v}^{\mathrm{H}}+\frac{Pr}{\gamma}\hat{T}^\dagger\hat{T}^{\mathrm{H}}\right). \tag{A10}$$

The distortion of the continuity equation gives rise to

$$\nabla_T^3\sigma=-\frac{\hat{p}^\dagger}{T^2}\left[\frac{dT}{dy}\hat{v}^{\mathrm{H}}+(\sigma^{\mathrm{H}}U+\mathrm{i}\omega)\hat{T}^{\mathrm{H}}\right]-\frac{d}{dy}\left(\frac{\hat{p}^\dagger\hat{v}^{\mathrm{H}}}{T}\right). \tag{A11}$$

The change in the pressure gradient term of the momentum equation yields

$$\nabla_T^4\sigma=-\frac{Re}{\mu^2}\frac{d\mu}{dT}\left[\sigma^{\mathrm{H}}\hat{u}^\dagger\hat{p}^{\mathrm{H}}+\frac{\hat{v}^\dagger}{l_2}\frac{d\hat{p}^{\mathrm{H}}}{dy}\right]. \tag{A12}$$

The variation in the base temperature gradient in the energy equation leads to

$$\nabla_T^5\sigma=-\frac{PrRe}{\gamma\mu T}\frac{d}{dy}\left(\hat{T}^\dagger\hat{v}^{\mathrm{H}}\right). \tag{A13}$$

The distortion of the viscous stress and dissipation terms gives

$$\nabla_T^6\sigma=\frac{1}{\mu}\frac{d\mu}{dT}\left[\frac{d}{dy}\left(\sigma^{\mathrm{H}}\hat{u}^\dagger\hat{v}^{\mathrm{H}}+\hat{u}^\dagger\frac{d\hat{u}^{\mathrm{H}}}{dy}+\hat{v}^\dagger\frac{d\hat{v}^{\mathrm{H}}}{dy}\right.\right.$$
$$\left.\left.+\sigma^{\mathrm{H}}\frac{l_0}{l_2}\hat{v}^\dagger\hat{u}^{\mathrm{H}}\right)\right]+\frac{1}{\mu}\frac{d^2\mu}{dT^2}\frac{dU}{dy}\frac{d\hat{u}^\dagger}{dy}\hat{T}^{\mathrm{H}}+\left(\frac{1}{\mu}\frac{d\mu}{dT}\right)^2\hat{u}^\dagger$$
$$\times\left(\frac{d^2U}{dy^2}\hat{T}^{\mathrm{H}}+\frac{dU}{dy}\frac{d\hat{T}^{\mathrm{H}}}{dy}\right)-\left[\frac{1}{\mu}\frac{d^2\mu}{dT^2}-\left(\frac{1}{\mu}\frac{d\mu}{dT}\right)^2\right]$$
$$\times\frac{dU}{dy}\hat{T}^{\mathrm{H}}\left[\frac{\sigma^{\mathrm{H}}}{l_2}\hat{v}^\dagger+(\gamma-1)PrMa^2\frac{dU}{dy}\hat{T}^\dagger\right]. \tag{A14}$$

The distortion of the heat conduction term yields

$$\nabla_T^7\sigma=\frac{1}{\mu^3}\frac{d\mu}{dT}\left\{\mu^2\left(\hat{T}^\dagger\frac{d^2\hat{T}}{dy^2}-\hat{T}^{\mathrm{H}}\frac{d^2\hat{T}^\dagger}{dy^2}\right)\right.$$
$$\left.+2\mu\left[\frac{d\mu}{dy}\frac{d}{dy}\left(\hat{T}^\dagger\hat{T}^{\mathrm{H}}\right)+\frac{d^2\mu}{dy^2}\hat{T}^\dagger\hat{T}^{\mathrm{H}}\right]-2\left(\frac{d\mu}{dy}\right)^2\hat{T}^\dagger\hat{T}^{\mathrm{H}}\right\}. \tag{A15}$$

The distortion of the pressure dilatation term contributes to

$$\nabla_T^8 \sigma = -\frac{(\gamma-1)PrRe}{\gamma\mu^2}\frac{d\mu}{dT}\left(\sigma^{\mathrm{H}}\hat{u}^{\mathrm{H}} + \frac{d\hat{v}^{\mathrm{H}}}{dy}\right)\hat{T}^{\dagger}. \tag{A16}$$

## REFERENCES


[1]S. Zuccher and P. Luchini, "Boundary-layer receptivity to external disturbances using multiple scales," Meccanica **49**, 441–467 (2014).
[2]D. C. Hill, "Adjoint systems and their role in the receptivity problem for boundary layers," J. Fluid Mech. **292**, 183–204 (1995).
[3]C. Airiau, S. Walther, and A. Bottaro, "Boundary layer sensitivity and receptivity," C. R. Méc. **330**, 259–265 (2002).
[4]A. Fedorov, A. Ryzhov, V. Soudakov, and S. Utyuzhnikov, "Receptivity of a high-speed boundary layer to temperature spottiness," J. Fluid Mech. **722**, 533–553 (2013).
[5]P. Luchini and A. Bottaro, "Görtler vortices: A backward-in-time approach to the receptivity problem," J. Fluid Mech. **363**, 1–23 (1998).
[6]G. Meneghello, P. J. Schmid, and P. Huerre, "Receptivity and sensitivity of the leading-edge boundary layer of a swept wing," J. Fluid Mech. **775**, R1 (2015).
[7]F. Giannetti and P. Luchini, "Structural sensitivity of the first instability of the cylinder wake," J. Fluid Mech. **581**, 167–197 (2007).
[8]P. Luchini, F. Giannetti, and J. Pralits, "Structural sensitivity of linear and nonlinear global modes," in *5th AIAA Theoretical Fluid Mechanics Conference* (AIAA, 2008), p. 4227.
[9]M. Natarajan, J. B. Freund, and D. J. Bodony, "Actuator selection and placement for localized feedback flow control," J. Fluid Mech. **809**, 775–792 (2016).
[10]P. Andersson, M. Berggren, and D. S. Henningson, "Optimal disturbances and bypass transition in boundary layers," Phys. Fluids **11**, 134–150 (1999).
[11]P. Luchini, "Reynolds-number-independent instability of the boundary layer over a flat surface: Optimal perturbations," J. Fluid Mech. **404**, 289–309 (2000).
[12]Y. Xi, J. Ren, L. Wang, and S. Fu, "Receptivity and stability of hypersonic leading-edge sweep flows around a blunt body," J. Fluid Mech. **916**, R2 (2021).
[13]P. Corbett and A. Bottaro, "Optimal perturbations for boundary layers subject to stream-wise pressure gradient," Phys. Fluids **12**, 120–130 (2000).
[14]P. Corbett and A. Bottaro, "Optimal linear growth in swept boundary layers," J. Fluid Mech. **435**, 1–23 (2001).
[15]P. Cathalifaud and P. Luchini, "Algebraic growth in boundary layers: Optimal control by blowing and suction at the wall," Eur. J. Mech.—B/Fluids **19**, 469–490 (2000).
[16]S. Walther, C. Airiau, and A. Bottaro, "Optimal control of Tollmien–Schlichting waves in a developing boundary layer," Phys. Fluids **13**, 2087–2096 (2001).
[17]G. Rigas, D. Sipp, and T. Colonius, "Nonlinear input/output analysis: Application to boundary layer transition," J. Fluid Mech. **911**, A15 (2021).
[18]A. Bottaro, P. Corbett, and P. Luchini, "The effect of base flow variation on flow stability," J. Fluid Mech. **476**, 293 (2003).
[19]J. Park and T. Zaki, "Sensitivity of high-speed boundary-layer stability to base-flow distortion," J. Fluid Mech. **859**, 476–515 (2019).
[20]O. Marquet, D. Sipp, and L. Jacquin, "Sensitivity analysis and passive control of cylinder flow," J. Fluid Mech. **615**, 221–252 (2008).
[21]L. Brandt, D. Sipp, J. O. Pralits, and O. Marquet, "Effect of base-flow variation in noise amplifiers: The flat-plate boundary layer," J. Fluid Mech. **687**, 503–528 (2011).
[22]A. Fedorov and A. Tumin, "High-speed boundary-layer instability: Old terminology and a new framework," AIAA J. **49**, 1647–1657 (2011).
[23]X. Tian, T. Liu, T. Wang, J. Zhu, and C. Wen, "Double-layer acoustic metasurface for the suppression of the Mack second mode in hypersonic boundary-layer flow," Phys. Fluids **34**, 074105 (2022).
[24]Q. Song and L. Zhao, "Scattering of mack modes by solid-porous junctions in hypersonic boundary layers," Phys. Fluids **34**, 084104 (2022).
[25]P. Guo, Z. Gao, C. Jiang, and C. Lee, "Sensitivity analysis on supersonic-boundary-layer stability subject to perturbation of flow parameters," Phys. Fluids **33**, 084111 (2021).
[26]X. Wang and D. Lallande, "Hypersonic boundary-layer stabilization using steady blowing and suction: Effect of forcing location," in *AIAA Scitech 2020 Forum* (AIAA, 2020), p. 2059.
[27]F. Miró Miró and F. Pinna, "Effect of uneven wall blowing on hypersonic boundary-layer stability and transition," Phys. Fluids **30**, 084106 (2018).
[28]V. Lysenko, S. Gaponov, B. Smorodsky, Y. G. Yermolaev, and A. Kosinov, "Influence of distributed heavy-gas injection on stability and transition of supersonic boundary-layer flow," Phys. Fluids **31**, 104103 (2019).
[29]S. B. Mamidala, A. Weingärtner, and J. Fransson, "Leading-edge pressure gradient effect on boundary layer receptivity to free-stream turbulence," J. Fluid Mech. **935**, A30 (2022).
[30]S. Liao, *Homotopy Analysis Method in Nonlinear Differential Equations* (Springer, 2012).
[31]H. Schlichting and K. Gersten, *Boundary-Layer Theory*, 9th ed. (Springer, New York, 2016).
[32]M. R. Malik, "Numerical methods for hypersonic boundary layer stability," J. Comput. Phys. **86**, 376–413 (1990).
[33]P. Guo, Z. Gao, C. Jiang, and C.-H. Lee, "Linear stability analysis on the most unstable frequencies of supersonic flat-plate boundary layers," Comput. Fluids **197**, 104394 (2020).
[34]L. M. Mack, "Linear stability theory and the problem of supersonic boundary-layer transition," AIAA J. **13**, 278–289 (1975).
[35]X. Tian and C. Wen, "Growth mechanisms of second-mode instability in hypersonic boundary layers," J. Fluid Mech. **908**, R4 (2021).
[36]Y. Zurigat, A. Nayfeh, and J. Masad, "Effect of pressure gradient on the stability of compressible boundary layers," AIAA J. **30**, 2204–2211 (1992).